Predictions and measurements of thermal conductivity of ceramic materials at high temperature

Zherui Han [1,*] Zixin Xiong [1,*] William T. Riffe [2] Hunter B. Schonfeld [3] Mauricio Segovia,[1] Jiawei Song,[4]
Haiyan Wang,[4] Xianfan Xu [1] Patrick E. Hopkins [3,2,5] Amy Marconnet [1,†] and Xiulin Ruan [1,‡]

[1]*School of Mechanical Engineering and the Birck Nanotechnology Center, Purdue University, West Lafayette, Indiana 47907-2088, USA*
[2]*Department of Materials Science and Engineering, University of Virginia, Charlottesville, Virginia 22904, USA*
[3]*Department of Mechanical and Aerospace Engineering, University of Virginia, Charlottesville, Virginia 22904, USA*
[4]*School of Materials Engineering, Purdue University, West Lafayette, Indiana 47907-2088, USA*
[5]*Department of Physics, University of Virginia, Charlottesville, Virginia 22904, USA*

The lattice thermal conductivity (κ) of two ceramic materials, cerium dioxide (CeO_2) and magnesium oxide (MgO), is computed up to 1500 K using first principles and the phonon Boltzmann transport equation (PBTE) and compared to time-domain thermoreflectance (TDTR) measurements up to 800 K. Phonon renormalization and the four-phonon effect, along with high-temperature thermal expansion, are integrated in our *ab initio* molecular dynamics calculations. This is done by first relaxing structures and then fitting to a set of effective force constants employed in a temperature-dependent effective potential method. Both three-phonon and four-phonon scattering rates are computed based on these effective force constants. Our calculated thermal conductivities from the PBTE solver agree well with the literature and our TDTR measurements. Other predicted thermal properties including thermal expansion, frequency shift, and phonon linewidth also compare well with the available experimental data. Our results show that high temperature softens phonon frequency and reduces four-phonon scattering strength in both ceramics. The temperature scaling law of κ is $\sim T^{-1}$ for three-phonon scattering only and remains the same after phonon renormalization. This scaling for three- plus four-phonon scattering is $\sim T^{-1.2}$, but is weakened to $\sim T^{-1}$ by phonon renormalization. This indicates that four-phonon scattering can play an important role in systems where measured κ decays with temperature as $\sim T^{-1}$, which was conventionally attributed to three-phonon only. Compared to MgO, we find that CeO_2 has a weaker four-phonon effect and renormalization greatly reduces its four-phonon scattering rates.

I. INTRODUCTION

High-temperature properties are important for many energy and power technologies primarily for two reasons. First, increasing the operating temperature can enhance the power generation or conversion efficiency [1], and potentially lower the cost of renewable energy [2]. Second, power generations involving thermochemical reactions usually require sufficiently high temperature to sustain appreciable power density [3]. Thermal transport in materials at high temperature ($\sim$1000 K or above) plays an indispensable role in these processes [3]. In particular, thermal barrier coatings (TBCs) [4] protect structural components, enabling them to survive the high operating temperature. Candidate materials for TBCs are usually ceramics as they have low thermal conductivity, high thermal stability, and appropriate thermal expansion behavior [3,5].

In dielectric solids, heat is mainly carried by phonons, i.e., the quantum mechanical description of lattice vibrations, and their dynamics can be described by the phonon

Boltzmann transport equation (PBTE) [6,7]. The thermal conductivity of ceramics is then limited by various inter-action processes, including intrinsic three-phonon scattering and scattering by defects and boundaries, as previously discussed in the work of Klemens and Gell [5]. In the recent decade, the advent of the first-principles technique, coupled with the PBTE, gives an accurate computation of phonon-phonon scattering rates and lattice thermal conductivity [8]. This approach, based on the lowest-order perturbation, i.e., three-phonon scattering, has achieved great success in predicting thermal properties [9–13]. However, theoretical models that work well at moderate temperatures face new challenges at high temperatures. Measurements at high temperatures on many technologically important materials such as silicon and diamond often report thermal conductivities that are lower than predicted [14]. On the other hand, another study reports nearly 50% underprediction in uranium oxide at 1500 K [15]. Measurements of phonon linewidth, a direct observation of optical phonon anharmonicity, show the opposite trend with temperature compared to predictions [16–18]. In light of these comparisons, higher-order anharmonicity is expected to have a significant impact on thermal transport [14,19,20]. This four-phonon effect is expected to be stronger at higher temperatures as it could scale quadratically with temperature [14]. Furthermore, phonon renormalization or the

---

*These authors contributed equally to this work.
†marconnet@purdue.edu
‡ruan@purdue.edu

finite-temperature effect is necessary to correct the potential landscape and renormalize the phonon energies when the traditional quasiharmonic approximation (QHA) fails [21,22]. High-temperature transport is likely to significantly deviate from what can be derived from QHA and needs to be considered from this different perspective. Several theoretical studies on highly anharmonic crystals have been devoted to integrating both four-phonon scattering and the finite-temperature effect [23,24]. These emerging theories motivate us to investigate high-temperature thermal transport in ceramics and extend the earlier theoretical understanding [5].

In this work, we combine *ab initio* molecular dynamics (AIMD) with the PBTE to evaluate the thermal properties of two ceramics, cerium dioxide (CeO_2) and magnesium oxide (MgO), at temperatures up to 1500 K. We compare our predicted thermal properties to available high-temperature experiments and our own time-domain thermoreflectance (TDTR) measurements from room temperature to 800 K. Investigated thermal properties include thermal expansion, optical phonon frequencies, phonon scattering rates (or linewidths), and thermal conductivity. Such detailed and comprehensive comparisons with experiments that are rarely seen in previous theoretical reports enable us to examine and verify different levels of physics. Note that the radiation component of thermal transport is not discussed here as we focus on lattice thermal conduction [5].

Through our first-principles calculations, we find that both CeO_2 and MgO have positive lattice thermal expansion. As temperature increases, the potential landscape is greatly affected: phonon frequencies are softened and phonon scattering rates are weakened. Comparison between the two ceramics shows that at high temperatures, the four-phonon effect is not strong for CeO_2 but well exceeds three-phonon scattering in MgO.

II. METHODOLOGY

A. Effect of temperature

We approach high-temperature thermal transport in solids with a comprehensive view. Solution of the PBTE gives us thermal conductivity κ in terms of the phonon mode-wise contribution,

$$\kappa = \sum_\lambda C_\lambda v_\lambda^2 \tau_\lambda, \quad (1)$$

where C_λ, v_λ, and τ_λ are the volumetric heat capacity, group velocity, and relaxation time for a phonon mode λ having momentum **q**. A temperature-dependent treatment without any prior assumptions requires that all elements in the calculation should be functions of temperature. In the above description, heat capacity is expressed as $C_\lambda = \frac{1}{V}[\partial(\hbar\omega n_\lambda^0)/\partial T] = \frac{k_B}{V}(\hbar\omega/k_B T)^2 n_\lambda^0(n_\lambda^0 + 1)$, which is a function of lattice volume V, temperature T, and phonon frequency ω. The phonon population at equilibrium obeys the Bose-Einstein distribution, $n_\lambda^0 = 1/(e^{(\hbar\omega/k_B T)} - 1)$, where k_B is the Boltzmann constant. The group velocity v_λ is determined by the phonon dispersion. The relaxation time τ_λ is the inverse of the scattering rate and can be computed by Fermi's golden rule. We write the scattering rate of a three-phonon absorption process $\Gamma_{\lambda\lambda'\lambda''}^{(+)}$ as

an example where one phonon λ absorbs another phonon λ' and emits a third phonon λ'' ($\lambda + \lambda' \rightarrow \lambda''$),

$$\Gamma_{\lambda\lambda'\lambda''}^{(+)} = \frac{\hbar\pi}{4} \frac{n_{\lambda'}^0 - n_{\lambda''}^0}{\omega_\lambda \omega_{\lambda'} \omega_{\lambda''}} |V_{\lambda\lambda'\lambda''}^{(+)}|^2 \delta(\omega_\lambda + \omega_{\lambda'} - \omega_{\lambda''})\Delta^{(+)}. \quad (2)$$

Conservation of energy is enforced by the Dirac delta function δ, and the matrix elements $V_{\lambda\lambda'\lambda''}^{(+)}$ are given by the Fourier transformation of third-order interatomic force constants Φ_3. The Kronecker delta $\Delta^{(+)} = \Delta_{\mathbf{q}+\mathbf{q}'+\mathbf{Q},\mathbf{q}''}$ describes the momentum conservation where **Q** is a reciprocal lattice vector with $\mathbf{Q} = 0$ implying a normal process. Similar expressions can be derived for four-phonon scattering with the computation of the fourth-order interatomic force constants Φ_4. The calculation of phonon scattering rates gives us the temperature dependence of τ_λ on phonon dispersion, phonon population, and force constants. Since phonon dispersion is solved by the dynamical matrix encoded in the harmonic force constants Φ_2, it is reasonable to argue that the temperature dependence of a thermal transport property $\rho(T)$ is some function (F) of lattice expansion, phonon population, and different orders of force constants in the current computational formalism, or

$$\rho(T) = F[n(T), V(T), \Phi_2(T), \Phi_3(T), \Phi_4(T)]. \quad (3)$$

Conventional theory with three-phonon scattering and ground-state first-principles calculations is essentially a simplified version of Eq. (3),

$$\rho(T) = F_{\text{conv}}[n(T), V(0\,\text{K}), \Phi_2(0\,\text{K}), \Phi_3(0\,\text{K})]. \quad (4)$$

This description gives a temperature dependence that is solely determined by the change of occupation number. A more reasonable description, given by Eq. (3), is that elevated temperature expands or shrinks the lattice, renormalizes the quasiparticle phonon energy, and changes the potential landscape in the system.

For the comparisons and discussions in later sections, we have calculated the set of force constants using a 0 K potential landscape, i.e., Φ_2, Φ_3, and Φ_4.

B. *Ab initio* molecular dynamics

As the operation temperatures that we define as "high temperatures" usually exceed the Debye temperature of ceramic materials, molecular dynamics simulation is suitable to describe the lattice dynamics. Simulations are carried out using the Vienna *Ab initio* Simulation Package (VASP) [25]. The first step of our calculation is to relax the structure at a certain temperature and get a new potential energy surface. Anharmonic force constants can then be evaluated on this new baseline. Under a constant-temperature, constant-pressure ensemble (NPT) with zero external pressure, the lattice relaxation is performed on a supercell structure constructed by $4 \times 4 \times 4$ primitive cells (192 atoms for CeO_2 and 128 atoms for MgO). On such a relaxed lattice, we switch to a constant-temperature, constant-volume ensemble (NVT). We employ a temperature-dependent effective potential (TDEP) method, detailed in Refs. [21,26], that collects the force-displacement dataset $\{\mathbf{F}_t^{\text{MD}}, \mathbf{U}_t^{\text{MD}}\}$ in productive N_t AIMD time steps to construct the effective harmonic force

constants Φ_2^*. These effective harmonic force constants are obtained by minimizing force differences in MD and a model harmonic system such that it can best describe the potential surface of a thermally excited lattice [21,26],

$$\min_{\Phi_2^*} \Delta \mathbf{F} = \frac{1}{N_t} \sum_{t=1}^{N_t} \left| \mathbf{F}_t^{\mathrm{MD}} - \mathbf{F}_t^{\mathrm{H}} \right|^2, \qquad (5)$$

where $\mathbf{F}_t^{\mathrm{H}}$ is the force calculated from effective harmonic system $\mathbf{F}_t^{\mathrm{H}} = \Phi_2^* \mathbf{U}_t^{\mathrm{MD}}$ in the t-th time step. A similar minimization process can extend to higher-order effective force constants by fitting the residual term in the harmonic system [27] and we are able to obtain a set of effective higher-order force constants Φ_3^* and Φ_4^*. In this work, the NVT simulation is performed 20 000 time steps to reach equilibrium and the extraction of effective force constants is performed on a final productive run of 2000 time steps.

C. Phonon scattering

Given a set of force constants describing the potential energy surface, the phonon scattering rates are computed by Fermi's golden rule. In this study, we consider both three-phonon (3ph) and four-phonon (4ph) scattering. The full expression for the scattering rate of one mode τ_λ^{-1} under the relaxation time approximation (RTA) is a summation of all the channels based on Matthiessen's rule [7],

$$\frac{1}{\tau_\lambda} = \frac{1}{N}\left(\sum_{\lambda'\lambda''}^{(+)} \Gamma_{\lambda\lambda'\lambda''}^{(+)} + \sum_{\lambda'\lambda''}^{(-)} \frac{1}{2}\Gamma_{\lambda\lambda'\lambda''}^{(-)} \right) + \frac{1}{N}\sum_{\lambda'}^{(\mathrm{iso})} \Gamma_{\lambda\lambda'}^{(\mathrm{iso})} + \frac{1}{N}\left(\sum_{\lambda'\lambda''\lambda'''}^{(++)} \frac{1}{2}\Gamma_{\lambda\lambda'\lambda''\lambda'''}^{(++)} + \sum_{\lambda'\lambda''\lambda'''}^{(+-)} \frac{1}{2}\Gamma_{\lambda\lambda'\lambda''\lambda'''}^{(+-)} + \sum_{\lambda'\lambda''\lambda'''}^{(--)} \frac{1}{6}\Gamma_{\lambda\lambda'\lambda''\lambda'''}^{(--)} \right), \qquad (6)$$

where N is the total number of grid points of $\mathbf{q}$ points when solving PBTE. The superscripts $(\pm)$ and $(\pm\pm)$ represent the 3ph and 4ph processes, respectively. The notations are for 3ph absorption ($\lambda + \lambda' \to \lambda''$) and emission ($\lambda \to \lambda' + \lambda''$), and 4ph recombination ($\lambda + \lambda' + \lambda'' \to \lambda'''$), redistribution ($\lambda + \lambda' \to \lambda'' + \lambda'''$), and splitting ($\lambda \to \lambda' + \lambda'' + \lambda'''$) processes. $\Gamma^{(\mathrm{iso})}$ is the isotope scattering rates. The calculation of Eq. (6) requires Φ_2^*, Φ_3^*, and Φ_4^* obtained from AIMD simulations and is performed in a modified version in our computational program, FOURPHONON [28]. In our calculation, the primitive cell of CeO_2 is sampled by a $10 \times 10 \times 10$ q mesh and that of MgO is sampled by a $12 \times 12 \times 12$ q mesh. More details on the first-principles calculations and force-constant evaluations can be found in the Supplemental Material [29], which also include Refs. [14,24,25,27,30–40].

D. TDTR measurement

We use time-domain thermoreflectance (TDTR) to characterize the thermal conductivity of MgO and CeO_2. A laser beam with a repetition rate of 80 MHz from a Ti:sapphire oscillator is split into pump and probe beams. The pulsed pump beam periodically heats the surface of the sample, which is coated with a thin ($\sim$80 nm) layer of Al transducer. A probe beam delayed up to 5.5 ns after heating by a pump pulse measures the change in reflectance due to the change in the temperature detected at the surface. The pump beam is modulated by an electro-optic modulator (EOM) at 8.4 MHz. The focused pump and probe beams have $1/e^2$ diameters of $\sim$19 and $\sim$10 μm, respectively. Each sample is coated with a thin layer of aluminum (the transducer layer), which serves to deposit the heating at the surface and enable measurement of the thermal response through a known dR/dT, where R is the surface reflectance. To obtain thermal conductivity and interface conductance, we fit both the magnitude ($\sqrt{V_{\mathrm{in}}^2 + V_{\mathrm{out}}^2}$) and the ratio ($\frac{V_{\mathrm{in}}}{V_{\mathrm{out}}}$) of the probe beam separately to a model of the response due to accumulative periodic heating by a pulsed laser [41–43]. Heat capacities and densities of materials are taken from the literature [39,44]. We fit the thermoreflectance response with two free parameters for the MgO substrate: the thermal conductivity of the substrate and the thermal conductance between the substrate and the transducer layer. For the CeO_2 thin film, there are three free parameters: the thermal conductivity of the film, the thermal conductance between the film and the transducer, and the thermal conductance between the film and the substrate. The sensitivity of the thermoreflectance response to each parameter is discussed in detail in the Supplemental Material [29]. To ensure repeatability, we record data on different days at several locations for each sample. Above room temperature, samples are heated and stabilized in a thermal stage with flowing argon gas to maintain a clean chamber environment.

III. RESULTS

Here, we present our first-principles results on various high-temperature thermal properties. In each section, we compare our results to the available experimental reports or our own measurements.

A. Thermal expansion

Figure 1 shows our calculated lattice constants as a function of temperature for both ceramics. We find that the lattice constant increases nearly linearly with temperature in CeO_2, resulting in a nearly constant thermal expansion coefficient, while the thermal expansion coefficient of MgO varies with temperature. The Debye temperature of CeO_2 is lower than that of MgO (750–890 K for MgO [49] and 466–484 K for CeO_2 [40]), so that the quantum effect altering the linearity of the thermal expansion is more pronounced in MgO. The predicted behaviors are consistent with experimental reports [45,46]. For CeO_2, the simulated linear thermal expansion coefficient is $\alpha = 1.05 \times 10^{-5}$ K^{-1}, while the experimental reported value is around 1.16×10^{-5} K^{-1} [45]. As for MgO, the trend with temperature is similar to the measured values as quantified by the linear thermal expansion coefficient shown in blue lines. But the absolute values of the lattice
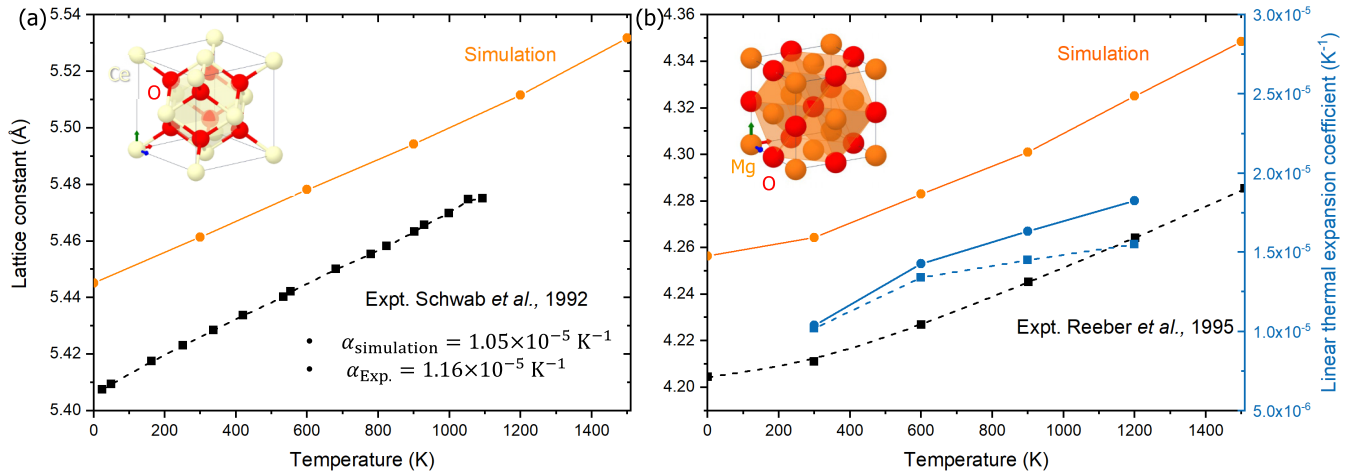
FIG. 1. Lattice constants of (a) CeO_2 and (b) MgO as a function of temperature. Simulation results are presented in orange solid lines, while experimental data [45,46] are in black with dashed lines to guide the eye. In the right panel, blue lines (simulation in solid line and experiment in dashed line) correspond to the linear thermal expansion coefficient of MgO in the right *y* axis that varies with temperature. Atomic structures in this figure are generated from a toolkit of MATERIALS PROJECT [47,48].

constants are off by a small fraction for both materials and it is likely due to an error in the ground state (0 K) structure determined by density functional theory (DFT). We note that the relative errors of the lattice constants are within 1.5% for both materials and such small difference is acceptable in first-principles calculations. For evaluation of the thermal properties, the agreement of thermal expansion behavior is more essential than the absolute lattice parameters.

B. Phonon dispersions

From the effective harmonic force constants Φ_2^* that are extracted from AIMD at each finite temperature, we can solve for phonon dispersions that are renormalized. Figure 2 presents our calculated phonon dispersions at 1500 K compared to 0 K. Since CeO_2 and MgO are both polar materials, longer-range interactions are needed to capture the splitting of transversal and longitudinal optical phonons (TO and LO modes) so that they are not degenerate at the Brillouin zone center. This interaction is computed using density functional perturbation theory (DFPT) and we get Born effective charge

tensor Z_{ij}^* and high-frequency dielectric constant ϵ_∞ for both materials.

Phonon energies are lower at higher temperature for all phonon modes in both materials. Our result is consistent with another theoretical study on CeO_2 [50], but differs from a recent theoretical paper on MgO [51] that reports phonon hardening. A very recent experimental study on MgO [35] reports phonon softening and supports our prediction on TO phonon frequency shift, as shown in Fig. 2(c). Earlier work [51] does not consider thermal expansion and we infer here that both thermal expansion and anharmonic contribution are needed to explain the frequency shift. We observe that the calculated frequency shift agrees better with the measured value at low temperatures, but is larger than the measured value at 1500 K. While we achieve agreement on the theory side for CeO_2, no data on optical phonon frequency shift are found in the literature for bulk single-crystal CeO_2. We note that past researchers evaluated nanopowders of CeO_{2-y} [52,53], but the confinement size effect that varies with heating cycles leads to mixed results on frequency shift.

We also compare our simulated sound velocity (group velocity of acoustic branches near the Γ point) to available
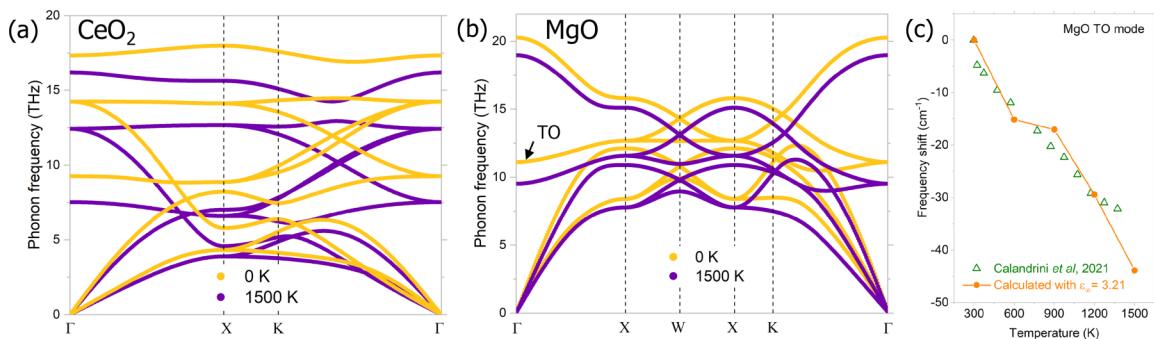

FIG. 2. Phonon dispersions at 0 and 1500 K for (a) CeO_2 and (b) MgO along high-symmetry paths. (c) Phonon frequency shift for the TO phonon mode of MgO as a function of temperature. Experimental data from Ref. [35] (green triangles) is compared to our calculated results (orange circles connected by orange lines). Note that our calculated high-frequency dielectric constant ϵ_∞ for MgO is 3.24.
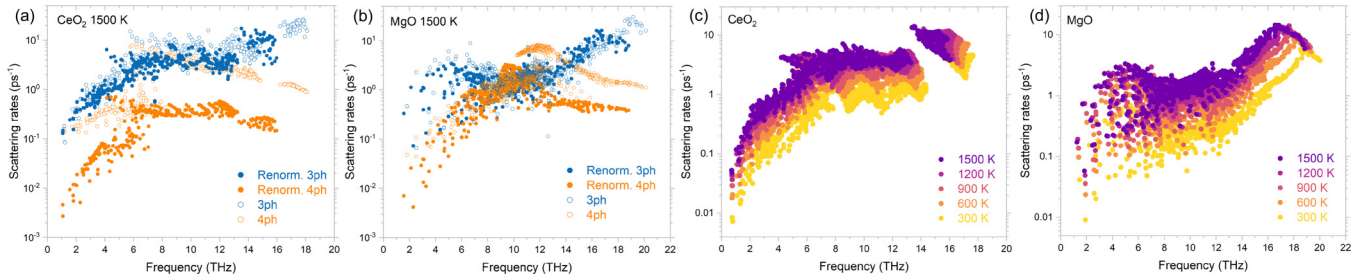
FIG. 3. Phonon scattering rates of (a),(c) CeO$_2$ and (b),(d) MgO as a function of phonon frequency. (a),(b) Phonon scattering rates at 1500 K including contributions from 3ph (blue circles) and 4ph (orange circles) scattering with and without phonon renormalization. Hollow circles are scattering rates calculated without phonon renormalization (that is, with Φ_2, Φ_3, and Φ_4), while filled circles include phonon renormalization (from the temperature-dependent Φ_2^*, Φ_3^*, and Φ_4^*). (c),(d) The temperature evolution of total phonon scattering rates considering both 4ph scattering and phonon renormalization. Different temperatures are represented by colors, with darker color indicating higher temperature.

experiments. For MgO, at the [110] direction, the group velocity is 5.9 km/s compared to the experimental value of 5.3 km/s [54]. For CeO$_2$, the group velocity is 3.6 km/s, while experiment gives 3.5 km/s [40].

C. Phonon scattering rates and linewidth

Next, we move to the evaluation of phonon anharmonicity. The renormalized phonon energy shows the temperature dependence of the real part of phonon self-energy; the scattering rates reveal its change in the imaginary part. In this study, we calculate both 3ph and 4ph scattering rates with the temperature-dependent Φ_2^*, Φ_3^*, and Φ_4^*. The results for both materials are summarized in Fig. 3. Figures 3(a) and 3(b) present 3ph and 4ph scattering rates at 1500 K and how these two channels are affected by phonon renormalization. The calculations with Φ_2, Φ_3, and Φ_4 (hollow circles) give high 4ph scattering rates that can be comparable or even overweigh 3ph scattering rates. The 4ph scattering strength scales quadratically with temperature [14], while 3ph scattering has a linear scaling relation, so that 4ph scattering generally becomes more important at higher temperature. However, our phonon renormalization approach with Φ_2^*, Φ_3^*, and Φ_4^* weakens 4ph scattering rates in both materials (see the difference between filled and hollow orange circles). The results for CeO$_2$ differ from MgO as renormalization makes 4ph scattering at least one magnitude lower than 3ph in CeO$_2$, while MgO still sees comparable 4ph scattering rates in the intermediate phonon frequency range. This observation suggests that the effect from phonon renormalization is material dependent. Another observation is that 3ph and 4ph scattering show different responses to phonon renormalization at finite temperature. We find a greater reduction in 4ph scattering rates than 3ph scattering when the phonon renormalization is applied.

In Figs. 3(c) and 3(d), we show the total phonon scattering rates at different temperatures up to 1500 K. The results are from temperature-dependent Φ_2^*, Φ_3^*, and Φ_4^*, where both 4ph scattering and phonon renormalization effects are included. For both materials, the general trend is increasing scattering with temperature, while the phonon spectrum shifts to lower frequencies (leftward) due to phonon softening at higher temperature. In addition, we find that the phonon mean free paths at 1500 K are mostly longer than the average interatomic

distance. This confirms the validity of the phonon gas model up to 1500 K in our simulations in the Supplemental Material [29].

While the whole spectrum phonon lifetime is not very accessible using current experimental techniques, a few optical phonon modes can be readily probed by Raman or infrared (IR) spectroscopy, providing some verification of the predicted trends. The linewidths of resonance peaks are caused by the anharmonic scattering of Raman/IR-active phonon modes, which are usually at the zone center, or phonon linewidth $\gamma = \frac{2\pi}{\tau}$ [55–57]. Comparing our simulated phonon linewidths to available measurements provides a good validation of our theory.

Figure 4 shows the TO phonon linewidth in MgO as a function of temperature. This mode is IR active and can
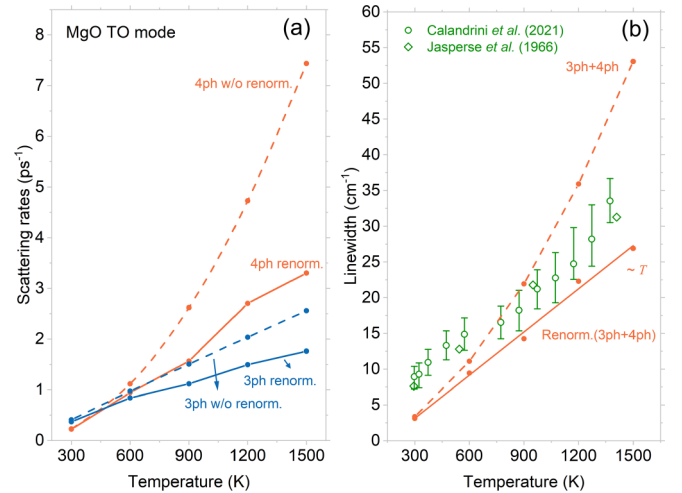

FIG. 4. Transverse optical phonon (a) scattering rates and (b) linewidth of MgO as a function of temperature. Scattering rates are calculated considering different phonon scattering mechanisms (3ph in blue circles and 4ph in orange circles). Data calculated *without* phonon renormalization (w/o renorm.) are connected by dashed lines, while those *with* phonon renormalization (renorm.) are connected by solid lines. Total phonon linewidths are compared to experiments (green circles [35] and diamonds [58]). Data calculated *without* phonon renormalization are connected by dashed lines, while those *with* phonon renormalization are connected by a linear fitting (solid line).

be detected by the infrared reflectivity measurement [35,58]. We first compare the calculated scattering rates from 3ph and 4ph scattering channels, with or without the effect of phonon renormalization [Fig. 4(a)]. Inspecting the difference between dashed lines and solid lines, the renormalization scheme reduces the scattering rates for both 3ph and 4ph scattering channels and such reduction is greater at higher temperature. Thus, this renormalization scheme is quite necessary for a high-temperature understanding. Inspecting the temperature dependence of phonon scattering, 4ph scattering is still more important at higher temperature and its contribution to linewidth starts to dominate at around 600 K for MgO. However, the previously assumed quadratic temperature dependence of 4ph scattering [14] is softened to be almost linear. The temperature scaling of 3ph scattering remains linear after renormalization. This results in a linear temperature dependence of total phonon linewidth up to 1500 K, as shown in Fig. 4(b), and our prediction incorporating both 4ph scattering and the phonon renormalization effect agrees well with a recent measurement [35] (presented in green open circles) and one historic literature data [58] (presented in green diamonds). The difference between our prediction and the experiments does not seem to be temperature dependent and could be attributed to finite resolution in the measurements and point defects in MgO samples. In contrast, without renormalization, 3ph+4ph scattering with Φ_2, Φ_3, and Φ_4 gives an overestimation of the phonon linewidth [dashed line in Fig. 4(b)], while 3ph scattering with Φ_2, Φ_3 underestimates the linewidth, as also discussed in Ref. [35]. Thus, only the theoretical consideration of 4ph scattering with phonon renormalization gives a reasonable agreement with the experiments.

D. Thermal conductivity

The lattice thermal conductivity κ is solved by the linearized PBTE [28,63] and, in this study, 3ph scattering is iterated while 4ph is treated at the RTA level. We compare our simulated results to our measurements using TDTR for a CeO_2 thin film with 900 nm thickness and an MgO substrate at high temperature, as well as to data from the literature.

For our TDTR measurements, examples of the fitted model to the measured data are shown in Fig. 5. The fitted models with $\pm 15\%$ perturbation on fitted thermal conductivity are plotted as dashed lines to illustrate sensitivity. To address the spot-to-spot variability and effects due to varying experimental setup conditions from day to day, we report the standard deviation of the best-fit values across measurements taken at various locations on different days as error bars in Fig. 6. Noise in the measured data is negligible as the measurements are clean.

Figure 6 summarizes our calculated results without and with renormalization (dashed and solid lines, respectively) compared with the literature data (black hollow symbols) and our own TDTR measurements (green squares). In both cases, we see a reduction in thermal conductivity when including the 4ph effects and the temperature dependence is further modified from $\sim T^{-1.2}$ to $\sim T^{-1}$ after phonon renormalization. In comparison, this temperature scaling relation of thermal
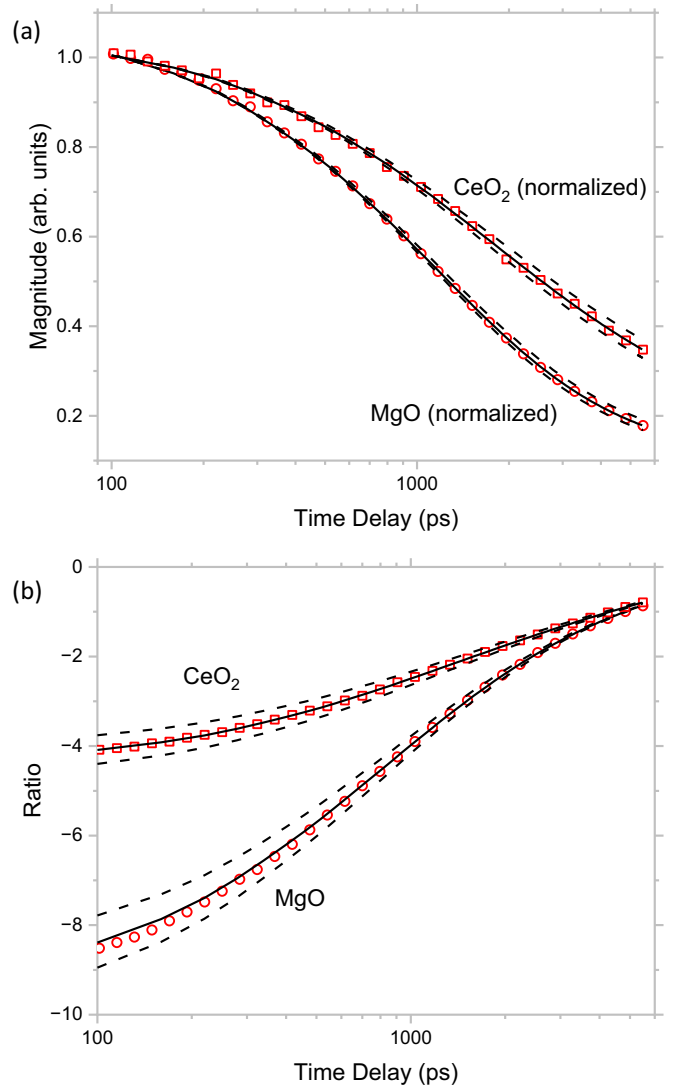

FIG. 5. (a) Normalized magnitude and (b) ratio of thermal response as a function of time delay for TDTR measurements of MgO (red circles) and CeO_2 (red squares), and the numerical fits (black solid lines) used to extract their thermal conductivity. The dashed lines correspond to $\pm 15\%$ variation in the fitted thermal conductivity. Note that the time delay is plotted on a logarithmic scale.

conductivity with 3ph scattering only remains $\sim T^{-1}$ after phonon renormalization.

For CeO_2, the predicted thermal conductivity increases when renormalization is considered for both 3ph and 3ph+4ph calculations. This is consistent with the observations in Fig. 3(a) where increasing temperature reduces 4ph scattering strength compared to the case without renormalization. Our results also align with the observations of prior studies [23,24,64], which show reduced scattering and increased thermal conductivity after renormalization.

Note that for CeO_2, the 3ph data [the scheme with Φ_2, Φ_3, or Φ_4 (dashed lines)] gives accidental agreements with some of the literature data [40,59], but that model does not provide a reasonable physical picture when we consider real experimental factors, as discussed below. Notably, the thermal conductivity of CeO_2 is strongly dependent on grain size
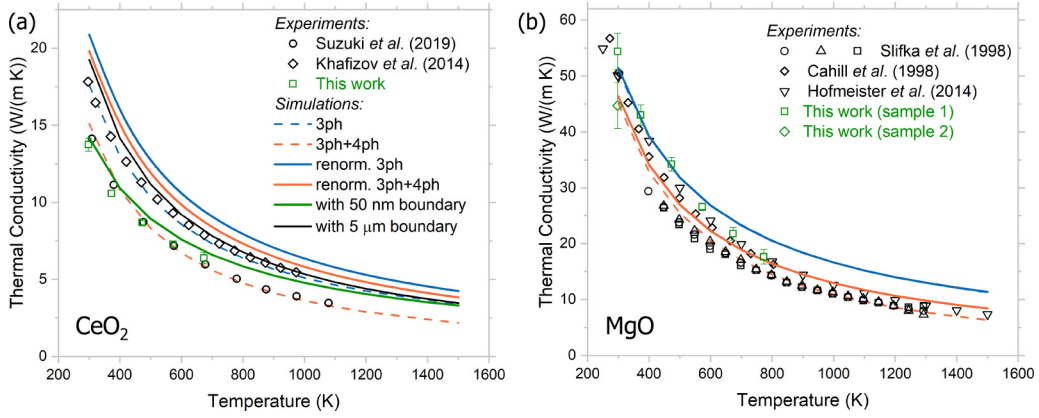
FIG. 6. Thermal conductivity κ as a function of temperature for (a) CeO_2 and (b) MgO. In (a), the experimental data from our TDTR measurements of a thin film of CeO_2 (green hollow squares) are compared to the literature values [from Ref. [40] (open circles) and Ref. [59] (open diamonds)]. In (b), experimental data for MgO in the literature (from Refs. [60–62] shown as black hollow symbols) are compared to our own TDTR measurements (green squares). For the simulation results, dashed lines show results *without* phonon renormalization and solid lines show results *with* phonon renormalization (3ph in blue and 3ph+4ph in orange). The solid green line in (a) represents the prediction with 50 nm characteristic length scale, while the black line represents the prediction with 5 μm boundary length. These simulation results are fitted into power law with temperature $\sim T^{-m}$.

and purity (both hard to control in the material fabrication process), while our simulations focus on single-crystal, pure materials. Khafizov *et al.* [59] observed a reduction in thermal conductivity from 17.5 W/(m K) for a pellet with 5 μm average grain diameter to 7.3 W/(m K) when the grain size decreases to 0.5 μm. Similarly, Suzuki *et al.* [40] found a 1% difference in purity level results in a more than 50% reduction in κ [from 14 W/(m K) to 6.1 W/(m K)]. Note that only the highest thermal conductivity results for each author are shown in Fig. 6(a) since our simulations are for pristine materials. We also evaluated a commercially available CeO_2 substrate sample (see the Supplemental Material [29] for more details). Due to the lack of measurements on a high-quality sample, we focus on our high-quality 900 nm film grown on a $SrTiO_3$ (STO) substrate by a pulsed laser deposition (PLD) method to compare with the predicted results.

To further validate our temperature-dependent prediction, we estimate the average grain size of our thin-film sample from x-ray diffraction (XRD) data to be between 40 and 65 nm. Thus, we compute a boundary scattering term [65],

$$\Gamma_b = \frac{2|v_\lambda^x|}{L}, \tag{7}$$

with characteristic length $L = 50$ nm and group velocity at the transport direction v_λ^x. The boundary scattering term Γ_b is added to the mode scattering rate τ_λ^{-1} in our solver and iterated with other scattering channels. The updated prediction with this boundary scattering is marked as a green solid line in Fig. 6(a) and agrees very well with our measurements on thin-film samples (shown as green hollow squares). We further calculate κ with the characteristic length reported in Ref. [59] (average grain size of 5 μm) and the results are shown as a solid black line in Fig. 6(a). The agreement is reasonable with a slightly larger difference at lower temperature.

For MgO [Fig. 6(b)], we find good consistency in the reported measurements and our experiment on the MgO substrate (MTI, Inc). Note that at room temperature, the

measurements contain data on two different samples. Each sample has consistently measured thermal conductivity. The difference in thermal conductivities between the two samples is attributed to the variation of samples in different batches from the vendor. Similar to CeO_2, including 4ph effects reduces thermal conductivity. But for MgO, including renormalization yields a small change in the thermal conductivity. Overall, all models give a reasonable agreement with the experiments given the fact that some previous experiments did not report the error bars. From 900 K and above, the scheme with Φ_2, Φ_3, and Φ_4 (dashed orange line) gives slightly lower κ than the experiments, while the theoretical prediction with Φ_2^*, Φ_3^*, and Φ_4^* well captures the high-temperature κ. In this high-temperature range, 3ph scattering only gives an overprediction of κ.

IV. CONCLUSION

In this study, we calculated the thermal properties of MgO and CeO_2 at temperature up to 1500 K by combining AIMD with the PBTE. The key to this scheme is computing the temperature-dependent force constants (Φ_2^*, Φ_3^*, and Φ_4^*, which are obtained from the TDEP method in this study). The calculated thermal properties are compared with experiments in the literature and our own measurements. Both materials are predicted to have positive thermal expansion with almost linear behavior for CeO_2 and temperature-dependent behavior for MgO due to the more pronounced quantum effect in MgO. The phonon frequencies soften for both materials with increasing temperature. We calculate both 3ph and 4ph scattering rates with temperature modification. Although 4ph scattering rates can be comparable to 3ph scattering rates at high temperature, our phonon renormalization approach weakens both 3ph and 4ph scattering strength. As a result, the phonon linewidths can have linear temperature dependence and our prediction explains the published data for an IR measurement on MgO. When both temperature dependence and renormalization are considered, the scattering rates of both

materials increase with temperature and the phonon spectrum shifts to lower frequencies due to phonon softening at high temperatures.

The predicted decreasing trend of thermal conductivity with temperature agrees well with experiments in the literature and our TDTR measurements. Due to the strong dependence on purity and grain size and other effects such as oxygen potential and stoichiometry, the experimentally determined thermal conductivity of CeO_2 is lower than our theoretical prediction. For CeO_2, the results agree well with our TDTR measurements of a thin-film sample when adding a 50 nm boundary scattering, comparable to the measured grain size, to the model including Φ_2^*, Φ_3^*, and Φ_4^*. Consistency between experimental measurements and predictions for bulk, single-crystal MgO is found, with the best agreement at high temperature, from the model including renormalized 3ph and 4ph scattering.

To conclude, through rigorous first-principles modeling and comprehensive comparisons with experiments on various thermal transport properties, we demonstrate the applicability of our methodology on high-temperature thermal transport in ceramics. In addition, this temperature-dependent approach can reveal the temperature evolution of thermal expansion, frequency shift, and linewidth broadening, which are not accessible or incorrectly described by conventional theory.

[1] J. H. Perepezko, The hotter the engine, the better, Science **326**, 1068 (2009).

[2] A. Henry and R. Prasher, The prospect of high temperature solid state energy conversion to reduce the cost of concentrated solar power, Energy Environ. Sci. **7**, 1819 (2014).

[3] S. Shin, Q. Wang, J. Luo, and R. Chen, Advanced materials for high-temperature thermal transport, Adv. Funct. Mater. **30**, 1904815 (2020).

[4] N. P. Padture, M. Gell, and E. H. Jordan, Thermal barrier coatings for gas-turbine engine applications, Science **296**, 280 (2002).

[5] P. G. Klemens and M. Gell, Thermal conductivity of thermal barrier coatings, Mater. Sci. Eng.: A **245**, 143 (1998).

[6] R. Peierls, On the kinetic theory of heat conduction in crystals, Ann. Phys. **395**, 1055 (1929).

[7] J. M. Ziman, *Electrons and Phonons: The Theory of Transport Phenomena in Solids*, International Series of Monographs on Physics (Clarendon Press, Oxford, 1960).

[8] D. A. Broido, M. Malorny, G. Birner, N. Mingo, and D. A. Stewart, Intrinsic lattice thermal conductivity of semiconductors from first principles, Appl. Phys. Lett. **91**, 231922 (2007).

[9] K. Esfarjani, G. Chen, and H. T. Stokes, Heat transport in silicon from first-principles calculations, Phys. Rev. B **84**, 085204 (2011).

[10] A. Seko, A. Togo, H. Hayashi, K. Tsuda, L. Chaput, and I. Tanaka, Prediction of low-thermal-conductivity compounds with first-principles anharmonic lattice-dynamics calculations and Bayesian optimization, Phys. Rev. Lett. **115**, 205901 (2015).

[11] L. Lindsay, D. A. Broido, and T. L. Reinecke, First-principles determination of ultrahigh thermal conductivity of boron arsenide: A competitor for diamond? Phys. Rev. Lett. **111**, 025901 (2013).

[12] L. Lindsay, C. Hua, X. L. Ruan, and S. Lee, Survey of *ab initio* phonon thermal transport, Mater. Today Phys. **7**, 106 (2018).

[13] A. J. H. McGaughey, A. Jain, H.-Y. Kim, and B. Fu, Phonon properties and thermal conductivity from first principles, lattice dynamics, and the Boltzmann transport equation, J. Appl. Phys. **125**, 011101 (2019).

[14] T. Feng, L. Lindsay, and X. Ruan, Four-phonon scattering significantly reduces intrinsic thermal conductivity of solids, Phys. Rev. B **96**, 161201(R) (2017).

[15] J. W. L. Pang, W. J. L. Buyers, A. Chernatynskiy, M. D. Lumsden, B. C. Larson, and S. R. Phillpot, Phonon lifetime investigation of anharmonicity and thermal conductivity of UO_2 by neutron scattering and theory, Phys. Rev. Lett. **110**, 157401 (2013).

[16] N. Bonini, M. Lazzeri, N. Marzari, and F. Mauri, Phonon anharmonicities in graphite and graphene, Phys. Rev. Lett. **99**, 176802 (2007).

[17] K. Kang, D. Abdula, D. G. Cahill, and M. Shim, Lifetimes of optical phonons in graphene and graphite by time-resolved incoherent anti-Stokes Raman scattering, Phys. Rev. B **81**, 165405 (2010).

[18] J. Lin, L. Guo, Q. Huang, Y. Jia, K. Li, X. Lai, and X. Chen, Anharmonic phonon effects in Raman spectra of unsupported vertical graphene sheets, Phys. Rev. B **83**, 125430 (2011).

[19] T. Feng and X. Ruan, Quantum mechanical prediction of four-phonon scattering rates and reduced thermal conductivity of solids, Phys. Rev. B **93**, 045202 (2016).

[20] Y. Xia, V. I. Hegde, K. Pal, X. Hua, D. Gaines, S. Patel, J. He, M. Aykol, and C. Wolverton, High-throughput study of lattice thermal conductivity in binary rocksalt and zinc blende compounds including higher-order anharmonicity, Phys. Rev. X **10**, 041029 (2020).

[21] O. Hellman, I. A. Abrikosov, and S. I. Simak, Lattice dynamics of anharmonic solids from first principles, Phys. Rev. B **84**, 180301(R) (2011).

[22] F. Zhou, W. Nielson, Y. Xia, and V. Ozoliņš, Lattice anharmonicity and thermal conductivity from compressive sensing of first-principles calculations, Phys. Rev. Lett. **113**, 185501 (2014).

[23] Y. Xia, Revisiting lattice thermal transport in PbTe: The crucial role of quartic anharmonicity, Appl. Phys. Lett. **113**, 073901 (2018).

[24] N. K. Ravichandran and D. Broido, Unified first-principles theory of thermal properties of insulators, Phys. Rev. B **98**, 085205 (2018).

[25] G. Kresse and J. Hafner, *Ab initio* molecular dynamics for liquid metals, Phys. Rev. B **47**, 558(R) (1993).

[26] O. Hellman, P. Steneteg, I. A. Abrikosov, and S. I. Simak, Temperature dependent effective potential method for accurate free energy calculations of solids, Phys. Rev. B **87**, 104111 (2013).

[27] O. Hellman and I. A. Abrikosov, Temperature-dependent effective third-order interatomic force constants from first principles, Phys. Rev. B **88**, 144301 (2013).

[28] Z. Han, X. Yang, W. Li, T. Feng, and X. Ruan, Four-Phonon: An extension module to ShengBTE for computing four-phonon scattering rates and thermal conductivity, Comput. Phys. Commun. **270**, 108179 (2022).

[29] See Supplemental Material at http://link.aps.org/supplemental/10.1103/PhysRevB.108.184306 for computational details, sample preparations and characterizations, and TDTR measurements.

[30] V. I. Anisimov, J. Zaanen, and O. K. Andersen, Band theory and Mott insulators: Hubbard U instead of Stoner I, Phys. Rev. B **44**, 943 (1991).

[31] C. Loschen, J. Carrasco, K. M. Neyman, and F. Illas, First-principles LDA+U and GGA+U study of cerium oxides: Dependence on the effective U parameter, Phys. Rev. B **75**, 035115 (2007).

[32] J. P. Perdew, K. Burke, and M. Ernzerhof, Generalized gradient approximation made simple, Phys. Rev. Lett. **77**, 3865 (1996).

[33] A. Togo and I. Tanaka, First principles phonon calculations in materials science, Scr. Mater. **108**, 1 (2015).

[34] S. Mochizuki, Infrared optical properties of cerium dioxide, Phys. Stat. Sol. (b) **114**, 189 (1982).

[35] E. Calandrini, L. Paulatto, D. Antonangeli, F. He, R. P. S. M. Lobo, F. Capitani, J.-B. Brubach, P. Roy, L. Vincent, and P. Giura, Limits of the quasiharmonic approximation in MgO: Volume dependence of optical modes investigated by infrared reflectivity and *ab initio* calculations, Phys. Rev. B **103**, 054302 (2021).

[36] J. Hu, X. Ruan, and Y. P. Chen, Thermal conductivity and thermal rectification in graphene nanoribbons: A molecular dynamics study, Nano Lett. **9**, 2730 (2009).

[37] M. T. Agne, R. Hanus, and G. J. Snyder, Minimum thermal conductivity in the context of diffusion-mediated thermal transport, Energy Environ. Sci. **11**, 609 (2018).

[38] Y. Luo, X. Yang, T. Feng, J. Wang, and X. Ruan, Vibrational hierarchy leads to dual-phonon transport in low thermal conductivity crystals, Nat. Commun. **11**, 2554 (2020).

[39] A. T. Nelson, D. R. Rittman, J. T. White, J. T. Dunwoody, M. Kato, and K. J. McClellan, An evaluation of the thermophysical properties of stoichiometric CeO$_2$ in comparison to UO$_2$ and PuO$_2$, J. Am. Ceram. Soc. **97**, 3652 (2014).

[40] K. Suzuki, M. Kato, T. Sunaoshi, H. Uno, U. Carvajal-Nunez, A. T. Nelson, and K. J. McClellan, Thermal and mechanical properties of CeO$_2$, J. Am. Ceram. Soc. **102**, 1994 (2019).

[41] C. A. Paddock and G. L. Eesley, Transient thermoreflectance from thin metal films, J. Appl. Phys. **60**, 285 (1986).

[42] A. Feldman, Algorithm for solutions of the thermal diffusion equation in a stratified medium with a modulated heating source, High Temp. High Press. **31**, 293 (1999).

[43] D. G. Cahill, Analysis of heat flow in layered structures for time-domain thermoreflectance, Rev. Sci. Instrum. **75**, 5119 (2004).

[44] L. S. Dubrovinsky and S. K. Saxena, Thermal expansion of periclase (MgO) and tungsten (W) to melting temperatures, Phys. Chem. Miner. **24**, 547 (1997).

[45] R. G. Schwab, R. A. Steiner, G. Mages, and H.-J. Beie, Properties of CeO$_2$ and CeO$_{2-x}$ films Part II. High temperature properties, Thin Solid Films **207**, 288 (1992).

[46] R. R. Reeber, K. Goessel, and K. Wang, Thermal expansion and molar volume of MgO, periclase, from 5 to 2900 K, Eur. J. Mineral. **7**, 1039 (1995).

[47] A. Jain, S. P. Ong, G. Hautier, W. Chen, W. D. Richards, S. Dacek, S. Cholia, D. Gunter, D. Skinner, G. Ceder, and K. A. Persson, Commentary: The materials project: A materials genome approach to accelerating materials innovation, APL Mater. **1**, 011002 (2013).

[48] S. P. Ong, W. D. Richards, A. Jain, G. Hautier, M. Kocher, S. Cholia, D. Gunter, V. L. Chevrier, K. A. Persson, and G. Ceder, Python materials genomics (PYMATGEN): A robust, open-source PYTHON library for materials analysis, Comput. Mater. Sci. **68**, 314 (2013).

[49] D. E. Gray, *American Institute of Physics Handbook* (McGraw-Hill, New York, 1957), pp. 4–47.

[50] J. Klarbring, N. V. Skorodumova, and S. I. Simak, Finite-temperature lattice dynamics and superionic transition in ceria from first principles, Phys. Rev. B **97**, 104309 (2018).

[51] C. Kwon, Y. Xia, F. Zhou, and B. Han, Dominant effect of anharmonicity on the equation of state and thermal conductivity of MgO under extreme conditions, Phys. Rev. B **102**, 184309 (2020).

[52] Z. V. Popović, Z. Dohčević-Mitrović, A. Cros, and A. Cantarero, Raman scattering study of the anharmonic effects in CeO$_{2-y}$ nanocrystals, J. Phys.: Condens. Matter **19**, 496209 (2007).

[53] S. D. Pandey, J. Singh, K. Samanta, N. D. Sharma, and A. K. Bandyopadhyay, Temperature dependent variations of phonon interactions in nanocrystalline cerium oxide, J. Nanomater. **2015**, 492967 (2015).

[54] O. L. Anderson and P. Andreatch, Jr., Pressure derivatives of elastic constants of single-crystal MgO at 23° and −195.8 °C, J. Am. Ceram. Soc. **49**, 404 (1966).

[55] M. Balkanski, R. F. Wallis, and E. Haro, Anharmonic effects in light scattering due to optical phonons in silicon, Phys. Rev. B **28**, 1928 (1983).

[56] J. Menéndez and M. Cardona, Temperature dependence of the first-order Raman scattering by phonons in Si, Ge, and α-Sn: Anharmonic effects, Phys. Rev. B **29**, 2051 (1984).

[57] X. Yang, T. Feng, J. S. Kang, Y. Hu, J. Li, and X. Ruan, Observation of strong higher-order lattice anharmonicity in

Raman and infrared spectra, Phys. Rev. B **101**, 161202(R) (2020).

[58] J. R. Jasperse, A. Kahan, J. N. Plendl, and S. S. Mitra, Temperature dependence of infrared dispersion in ionic crystals LiF and MgO, Phys. Rev. **146**, 526 (1966).

[59] M. Khafizov, I.-W. Park, A. Chernatynskiy, L. He, J. Lin, J. J. Moore, D. Swank, T. Lillo, S. R. Phillpot, A. El-Azab, and D. H. Hurley, Thermal conductivity in nanocrystalline ceria thin films, J. Am. Ceram. Soc. **97**, 562 (2014).

[60] A. J. Slifka, B. J. Filla, and J. M. Phelps, Thermal conductivity of magnesium oxide from absolute, steady-state measurements, J. Res. Natl. Inst. Stand. Technol. **103**, 357 (1998).

[61] A. M. Hofmeister, Thermal diffusivity and thermal conductivity of single-crystal MgO and Al_2O_3 and related compounds as a function of temperature, Phys. Chem. Miner. **41**, 361 (2014).

[62] D. G. Cahill, S.-M. Lee, and T. I. Selinder, Thermal conductivity of κ-Al_2O_3 and α-Al_2O_3 wear-resistant coatings, J. Appl. Phys. **83**, 5783 (1998).

[63] W. Li, J. Carrete, N. A. Katcho, and N. Mingo, ShengBTE: A solver of the Boltzmann transport equation for phonons, Comput. Phys. Commun. **185**, 1747 (2014).

[64] X. Yang, J. Tiwari, and T. Feng, Reduced anharmonic phonon scattering cross-section slows the decrease of thermal conductivity with temperature, Mater. Today Phys. **24**, 100689 (2022).

[65] N. Mingo and D. A. Broido, Length dependence of carbon nanotube thermal conductivity and the "problem of long waves," Nano Lett. **5**, 1221 (2005).